



Rock salt type NiCo_2O_3 supported on ordered mesoporous carbon as a highly efficient electrocatalyst for oxygen evolution reaction

Yan Zhang^{a,1}, Xiuxiu Wang^{a,1}, Fenqiang Luo^b, Yang Tan^a, Lingxing Zeng^{b,*}, Baizeng Fang^{c,*}, Aihua Liu^{a,*}

^a Institute for Biosensing, and College of Life Sciences, and College of Chemistry & Chemical Engineering, Qingdao University, Qingdao, 266071, China

^b College of Environmental Science and Engineering, Fujian Key Laboratory of Pollution Control & Resource Reuse, Fujian Normal University, Fuzhou, Fujian 350007, China

^c Clean Energy Research Centre, Department of Chemical and Biological Engineering, University of British Columbia, 2360 East Mall, Vancouver, BC, V6P 1Z3, Canada

ARTICLE INFO

Keywords:

Rock salt type $\text{Ni}_x\text{Co}_y\text{O}_{x+y}$
Ordered mesoporous carbon
Carbon thermal reduction
Electrocatalyst
Oxygen evolution reaction

ABSTRACT

It is a great challenge to develop cost-effective and stable oxygen evolution reaction (OER) electrocatalysts for energy sustainability. Herein, we report nanocomposites of rock salt type nickel oxide and cobalt oxide supported on ordered mesoporous carbon (OMC) as efficient non-noble metal electrocatalysts for the OER in alkaline solution. The rock salt type $\text{Ni}_x\text{Co}_y\text{O}_{x+y}$ @OMC ($x/y = 0:1, 2:1, 1:1, 1:2, 1:0$) nanocomposites are synthesized through a nanocasting and carbon thermal reduction route by using the OMC as a nano-reactor. The OMC is used as the support material, with large specific surface area and pore volume, which can not only effectively disperse metal oxides nanoparticles and prevent the agglomeration of nanoparticles, but also improve electrocatalytic performance of metal oxides by increasing electrical conductivity and electrocatalytic active sites. Interestingly, the rock salt type NiCo_2O_3 @OMC exhibits the lowest overpotential of 281 mV at 10 mA/cm² in 1 M KOH, which is even lower than those values reported previously for RuO_2 and IrO_2 precious catalysts, and a small Tafel slope of 96.8 mV/dec for the OER. Notably, the NiCo_2O_3 @OMC has a turnover frequency value of 0.0341 s⁻¹ and an actual oxygen generation rate of ca. 22.5 μmol/h, much higher than its counterparts, confirming its outstanding intrinsic activity as an OER catalyst. Furthermore, the NiCo_2O_3 @OMC has a good durability without obvious attenuation after continuous operation test for 230 h. Evidently, the NiCo_2O_3 @OMC catalyst can remarkably promote the OER, and thus brighten the prospect of non-noble metal for efficient water electrolysis in industrial scale.

1. Introduction

As the increasing global warming and climate change issues continue, researchers have devoted great efforts to developing less expensive, environmentally benign, relatively nontoxic electrocatalysts for sustainable energy storage and conversion [1–7]. Electrocatalytic water splitting involves anodic oxygen evolution reaction (OER) and cathodic hydrogen evolution reaction [6–11], which is very restricted for practical application due to its serious overpotential requirements [9,7–11]. Especially, the inherently sluggish kinetics of the OER process involves multi-electron transfer steps, significantly lowering the efficiency of energy conversion [12]. Ruthenium oxide (RuO_2) and iridium oxide (IrO_2) [13,14] are the state-of-art OER electrocatalysts, however, their widespread applications in industry are greatly hindered by their

high prices and poor stability [15]. Hence, the development of inexpensive, highly active and stable electrocatalysts for water splitting remains a great challenge.

In the past decades, transition metal oxides are widely studied in alkaline electrolytes and have been regarded as effective candidate electrocatalysts for water splitting [16]. To date, a number of materials based on iron (Fe), cobalt (Co), and nickel (Ni) oxides have been developed as efficient OER electrocatalysts. In particular, cobalt-based oxides [17,18] are the most promising OER electrocatalysts owing to their high activity, low price, and good stability. In addition, doping with metal element, such as Fe, Zn, Cu and Ni can boost the catalytic activity of cobalt-based oxides. Among these doping elements, Ni doping can enable cobalt-based oxides to possess the highest electronic conductivity and abundant active sites for water splitting [19]. In

* Corresponding authors.

E-mail addresses: zenglingxing@fjnu.edu.cn (L. Zeng), bfang@chbe.ubc.ca (B. Fang), liuah@qdu.edu.cn (A. Liu).

¹ These authors contributed equally to this work.

addition, the Ni and Co species can interact with water to form M–O (M=Ni or Co) bonds [20] and accordingly facilitate water splitting. Furthermore, Ni-Co oxide-based materials have revealed superior OER performance to that of any single oxide (Ni or Co) [21,22]. Recent progress has manifested that rock salt type NiO-CoO solid solutions are a promising non-precious active electrocatalyst for the overall water splitting because of their optical and other properties [23]. However, it is challenging to synthesize rock salt type NiO-CoO nanocomposites with varying ratios by the traditional methods, in spite of the structural similarity, and generally more thermodynamically stable phases (Ni-doped Co_3O_4 or NiCo_2O_4) or phase mixtures are obtained. Therefore, facile fabrication of rock salt type NiO-CoO structure is highly desirable. Furthermore, metal oxides species with inherent low conductivity may hinder the charge transfer, and greatly affect the electrocatalytic activity towards the OER in practical applications. Fortunately, this disadvantage can be greatly improved by introducing carbon materials such as graphene [24,25] and carbon nanotubes [26] because of their high electrical conductivity.

Mesoporous carbons, as a new class of non-silicon-based mesoporous material, have excellent conductivity, chemical stability, large specific surface area and pore volume, and are ideal substrates to produce composite materials for various applications. Particularly, ordered mesoporous carbon (OMC) is very promising for electrochemical hydrogen storage [27] and other electrochemical energy applications. Among the composites of carbon supported transition metal oxides, NiFeO_x [28,29], MnCo_2O_4 [30,31] and CeO_2 [32,33] grown on mesoporous carbons have been frequently studied in order to facilitate the OER performance in water splitting. Nevertheless, to the best of our knowledge, rock salt type NiO-CoO supported on OMC has not been reported previously.

In this contribution, we present rock salt type Ni-Co oxides with different Ni/Co molar ratios supported on OMC ($\text{Ni}_x\text{Co}_y\text{O}_{x+y}\text{@OMC}$) as the OER electrocatalysts for water splitting. $\text{Ni}_x\text{Co}_y\text{O}_{x+y}\text{@OMC}$ nanocomposites were fabricated through a nanocasting and carbon thermal reduction route by using the OMC as a nano-reactor. The introduced OMC can not only provide a large surface area for the homogeneous growth of the metal oxides, but also promote electrons pass through the catalyst layer efficiently. The rock salt type $\text{NiCo}_2\text{O}_3\text{@OMC}$ has exhibited the lowest OER overpotential of 281 mV at 10 mA/cm^2 in 1 M KOH, which is lower than those values of RuO_2 and IrO_2 precious catalysts, and a small Tafel slope of 96.8 mV/dec. Additionally, the $\text{NiCo}_2\text{O}_3\text{@OMC}$ has a turnover frequency value of 0.0341 s^{-1} , much higher than its counterparts. It is worth mentioning that the OMC can act as a promising nanoreactor for fabricating and accommodating ultrasmall Ni-Co oxides nanoparticles. Consequently, tailoring $\text{Ni}_x\text{Co}_y\text{O}_{x+y}\text{@OMC}$ composites with a hybrid structure could lead to an outstanding electrocatalyst for the OER.

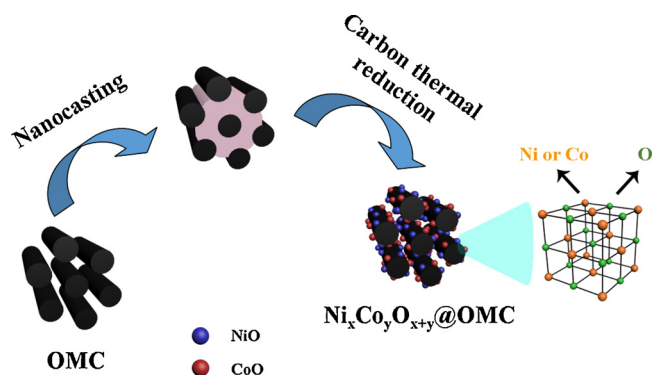
2. Experimental section

2.1. Chemicals and materials

OMC was synthesized according to the literatures [34,35]. All chemicals and materials, including nickel nitrate ($\text{Ni}(\text{NO}_3)_2 \cdot 6\text{H}_2\text{O}$), cobalt nitrate ($\text{Co}(\text{NO}_3)_2 \cdot 6\text{H}_2\text{O}$), nitric acid (HNO_3), potassium hydroxide (KOH), poly(acrylic acid) and Nafion were purchased from Aladdin chemical company and used without further purification. All aqueous solutions were prepared with Milli-Q water (18 $\text{M}\Omega \cdot \text{cm}$).

2.2. Preparation of $\text{Ni}_x\text{Co}_y\text{O}_{x+y}\text{@OMC}$ composites

As shown in Scheme 1, m mmol ($m = 0, 0.89, 0.67, 0.44, 0.75$) of $\text{Ni}(\text{NO}_3)_2 \cdot 6\text{H}_2\text{O}$ and n mmol ($n = 0.75, 0.45, 0.67, 0.89, 0$) of $\text{Co}(\text{NO}_3)_2 \cdot 6\text{H}_2\text{O}$ were dissolved in 10 mL of ethanol to form a homogeneous mixture solution. 0.1 g of OMC was introduced into 5 mL of 2 M HNO_3 solution under stirring at 60 °C for 0.5 h. After that, 0.1 g of



Scheme 1. Cartoon illustrating preparation route of $\text{Ni}_x\text{Co}_y\text{O}_{x+y}\text{@OMC}$ nanocomposites.

OMC powder was added into the mixture solution and treated with ultrasound for 2 h. Then, the mixture was stirred until the solution dried naturally. Finally, the sample was calcinated at 350 °C for 6 h under Ar atmosphere. Different compositions of NiO/CoO ultrasmall nanoparticles were loaded onto the OMC carbon matrix by impregnation of the precursor solution, followed by a carbon thermal reduction route. The corresponding products are labeled as $\text{Ni}_x\text{Co}_y\text{O}_{x+y}\text{@OMC}$ ($x/y = 0:1, 2:1, 1:1, 1:2, 1:0$).

2.3. Characterization

The structure and morphology of the samples were recorded by X-ray diffraction (XRD, D/Max-2500 pc diffractometer) with Cu K α radiation ($\lambda = 0.154056 \text{ nm}$) and transmission electron microscope (TEM, FEI F20 S-TWIN). Nitrogen adsorption-desorption isotherms were tested by Micromeritics ASAP 2020 instrument, and Brunauer-Emmett-Teller (BET) surface area was determined from the nitrogen isotherm curves. The pore size distribution of the as-prepared samples was obtained using Barrett-Joyner-Halenda (BJH) method. The metal content of the $\text{Ni}_x\text{Co}_y\text{O}_{x+y}\text{@OMC}$ was determined by using an Inductively Coupled Plasma-Optical Spectrometer (ICP-OES, Thermo ICAP 6300 Radial). X-ray photoelectron spectroscopy (XPS, ESCALAB 250Xi, Al K α radiation source) was used to examine the surface elemental composition of the samples. Raman spectra were measured with a Renishaw Raman microscope by a laser of 532 nm wavelength.

2.4. Electrochemical measurements

Electrochemical measurements were carried out on AUTOLAB PGSTAT302N electrochemical workstation (Metrohm, Switzerland) using a three-electrode electrochemical system at room temperature in 1 M KOH aqueous solution. The working electrode was prepared as follows: 2 mg of the as-prepared electrocatalyst was dispersed in 0.5 mL of poly(acrylic acid) (1 mg/mL), followed by ultrasonication for 20 min to obtain a homogeneous suspension. Afterward, 10 μL of the catalyst ink was dropped on the surface of a glassy carbon electrode (GCE, 3 mm in diameter) and dried at room temperature, and finally, 10 μL of 0.1 wt % Nafion was covered on the surface of catalyst. In other words, the homogeneous ink was spread out on the GCE surface with a mass loading of 0.567 mg/cm^2 for the OER. The as-prepared modified GCE, Ag/AgCl electrode, and carbon rod were used as working electrode, reference electrode and counter electrode, respectively. All potentials in this work were referred to reversible hydrogen electrode (RHE). In 1 M KOH, $E \text{ (vs. RHE)} = E \text{ (vs. Ag/AgCl)} + (0.197 + 0.059 \times \text{pH}) \text{ V}$. The electrochemical performance of the catalysts towards the OER was examined by linear sweep voltammetry (LSV) with a scan rate of 5 mV/s. Chronoamperometry (CA) was carried out at 1.5 V to investigate the stability of electrocatalysts for the OER. The Electrochemical impedance spectroscopy (EIS) of the samples was carried out in the

frequency range from 10^5 to 10^{-2} Hz with an AC voltage of 5 mV.

2.5. Calculation of turnover frequency of the catalysts

The turnover frequency (TOF) is determined by assuming that all metal atoms are included in the electrocatalytic processes [36,37]. The TOF value can be calculated based on the formula: $\text{TOF} = (j \times A) / (4 \times F \times n)$ [36,37], where j (mA/cm²) is the current density, A is the surface area of GCE (3 mm in diameter), the number 4 indicates the number of electrons involved in the formation of 1 mol O₂, F is the Faraday's constant (96485.3 C/mol), and n represents the moles of metal atoms of the catalysts on the electrode.

3. Results and discussion

3.1. Surface characterizations of the rock salt type Ni-Co oxides

With the OMC as a nanoreactor, rock salt type Ni-Co oxides with different Ni/Co molar ratios (i.e., 0:1, 2:1, 1:1, 1:2, 1:0) were loaded with ultrasmall nanoparticles which are denoted as Ni_xCo_yO_{x+y}@OMC nanocomposites ($x:y = 0:1, 1:2, 1:1, 2:1, 1:0$, respectively). The actual contents of Ni and Co of the nanocomposites were determined and confirmed by ICP-OES analysis (Table S1, Supplementary Information), which are consistent with the Ni/Co ratios set for the preparation of the nanocomposites.

The XRD patterns of the OMC and Ni_xCo_yO_{x+y}@OMC composites

($x:y = 0:1, 1:2, 1:1, 2:1, 1:0$) are shown in Fig. 1. The XRD pattern of the OMC reveals only one broadened diffraction peak at 2θ of 27°, indicating the amorphous characteristics of the OMC. All the other samples display three broad diffraction peaks, which can be indexed to the cubic rock salt structure CoO (JCPDS 89-7099) and NiO (JCPDS 89-3080), implying a high purity of CoO and NiO without the presence of other phase [38–40]. All of the Ni_xCo_yO_{x+y}@OMC composites ($x:y = 1:0, 2:1, 1:1, 1:2, 0:1$) show the broad diffraction peaks, indicating the ultra-small size of the NiO or CoO nanoparticles. As shown in Fig. 1B, the magnified (111) and (200) diffraction peaks display obvious shift for the Ni_xCo_yO_{x+y}@OMC composites ($x:y = 1:0, 2:1, 1:1, 1:2, 0:1$) to lower angles with the increasing Co content, suggesting partial incorporation of Co into the NiO structure. Generally, peak splits can be observed when NiO and CoO are separate phases (Fig. S1) [41]. According to the Scherrer equation ($D = k\lambda/\beta\cos\theta$) [11,42], the mean particle size of the NiCo₂O₃@OMC was calculated to be ca. 4.0 nm based on the (200) plane.

Fig. 1C and 1D display the nitrogen adsorption-desorption isotherms and pore size distributions of the Ni_xCo_yO_{x+y}@OMC composites ($x:y = 0:1, 1:2, 1:1, 2:1, 1:0$) and OMC, respectively. It is clear that all the samples displayed type IV isotherms with H1-type hysteresis loop, which is typical for mesoporous materials. The surface area and total pore volume of the OMC are 1268 m²/g and 1.33 cm³/g, respectively, which are much higher than those of the Ni_xCo_yO_{x+y}@OMC composites, as shown in Table S2, indicating that the Ni-Co oxides nanoparticles were confined into the meso-channels of ca. 4.1 nm of the

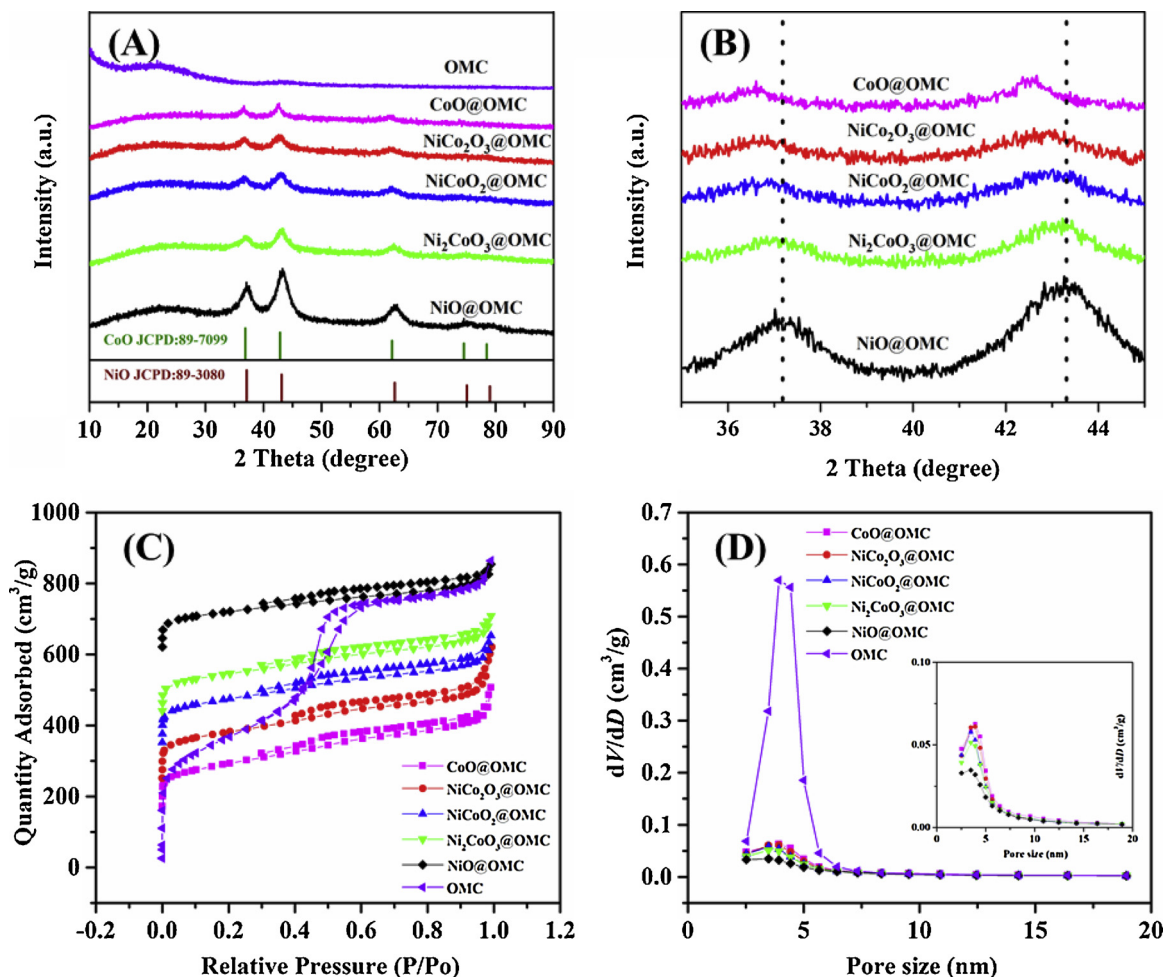


Fig. 1. (A) XRD patterns of the OMC and Ni_xCo_yO_{x+y}@OMC nanocomposites ($x:y = 0:1, 1:2, 1:1, 2:1, 1:0$). (B) Magnification of the (111) and (200) diffraction peaks showing obvious shift of the patterns. (C) Nitrogen adsorption-desorption isotherms and (D) pore size distributions of the Ni_xCo_yO_{x+y}@OMC composites ($x:y = 0:1, 1:2, 1:1, 2:1, 1:0$) and OMC. Pore size distributions from the adsorption branch through the BJH method.

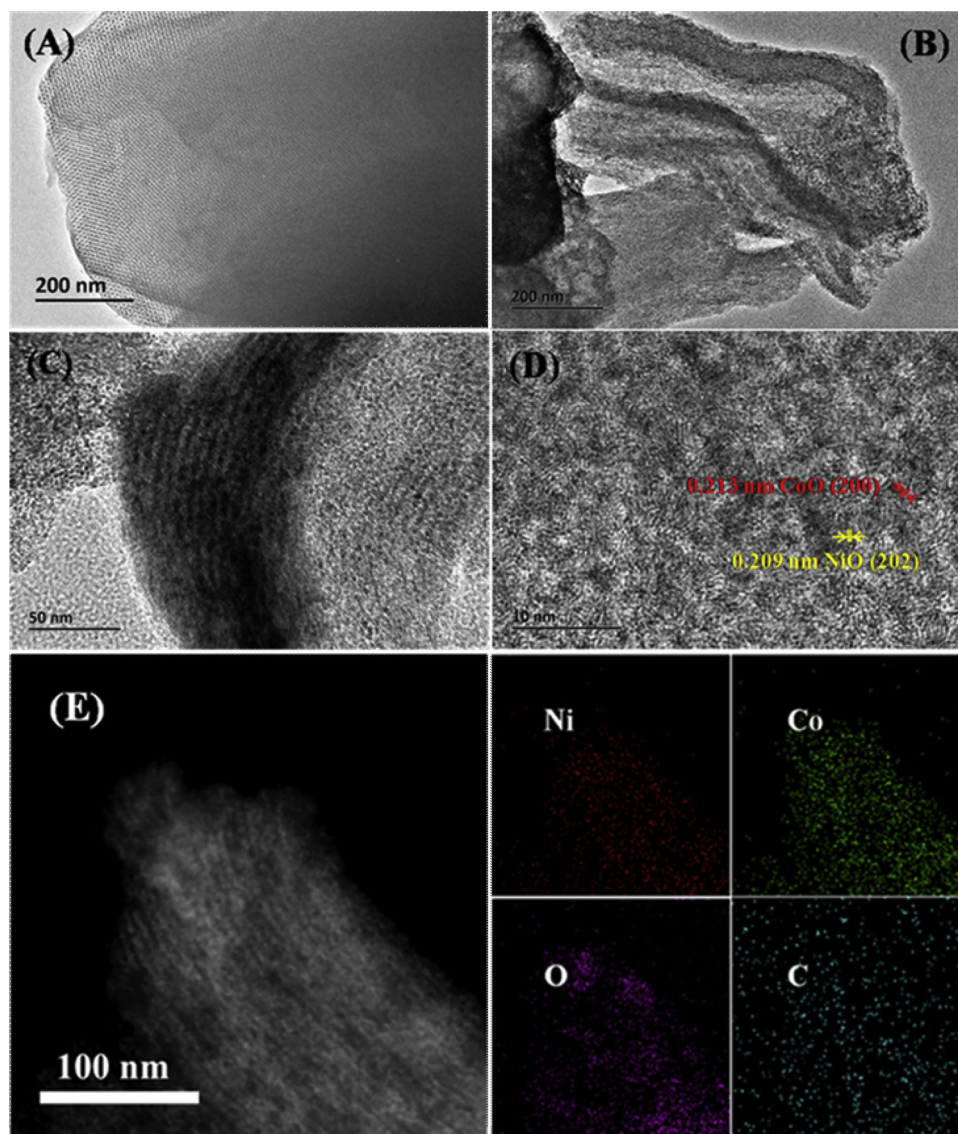


Fig. 2. TEM images of OMC (A) and NiCo_2O_3 @OMC (B, C) nanocomposite. (D) high-resolution TEM image of NiCo_2O_3 @OMC nanocomposite. (E) Dark field TEM image of the NiCo_2O_3 @OMC nanocomposite and the corresponding elemental mappings of Ni, Co, O and C.

OMC [43]. It is also found that the pore diameter of the NiCo_2O_3 @OMC is slightly larger than those of the $\text{Ni}_x\text{Co}_y\text{O}_{x+y}$ @OMC composites ($x:y = 1:1, 2:1$).

The TEM image of the OMC shows a regular pore arrangement and uniform channels (Fig. 2A) [44]. Fig. 2B and 2C represent the TEM images of the as-synthesized NiCo_2O_3 @OMC. Obviously, many ultra-small nanoparticles of NiCo_2O_3 were anchored on the surface of OMC, and no evident aggregation of the nanoparticles in the OMC matrix was observed. Meanwhile, the HRTEM image further confirmed the Ni-Co oxides were formed on the OMC and the size of the Ni-Co oxide nanoparticles was about 3–6 nm (Fig. 2D), which is in agreement with the results of XRD analysis. Besides, some lattice fringes can be observed, and the d-spacing values calculated were consistent well with CoO (200) and NiO (202). These results prove that the OMC can act as a promising nanoreactor to fabricate and accommodate ultra-small Ni-Co oxides nanoparticles.

Fig. 2E shows the dark field TEM image and elemental mapping of Ni, Co, O and C of the NiCo_2O_3 @OMC. As evident in the mapping photographs, the distribution of Ni and Co elements was very uniform, indicating that the Ni-Co oxide nanoparticles were uniformly dispersed onto the OMC matrix. Moreover, the corresponding energy-dispersive

spectroscopy (EDS) from TEM was used to analyze chemical elements of the NiCo_2O_3 @OMC. The EDS result confirmed that Ni and Co elements in the NiCo_2O_3 @OMC were detected (Fig. S2). In addition, Cu element also appeared in Fig. S2, because a Cu sheet was used during the EDS test. Evidently, the ultra-small Ni-Co oxides nanoparticles supported on the OMC have been successfully prepared by using the OMC as the nanoreactor.

Raman spectra of the $\text{Ni}_x\text{Co}_y\text{O}_{x+y}$ @OMC composites ($x:y = 1:0, 2:1, 1:1, 1:2, 0:1$) are displayed in Fig. 3A. The two strong peaks observed at 1338 and 1593 cm^{-1} were identified as D and G bands of the mesoporous carbon, respectively. The Raman peak of the NiO@OMC at 498.2 cm^{-1} can be ascribed to the one-phonon longitudinal optic (Lo) mode of NiO [45]. The sharp Raman peak of the CoO@OMC located at 678.6 cm^{-1} corresponds to A_{1g} phonon modes of CoO [46]. Compared with the NiO@OMC reference, the peak positions of the $\text{Ni}_x\text{Co}_y\text{O}_{x+y}$ @OMC composites ($x:y = 2:1, 1:1, 1:2$) also exhibited obvious shifts to larger wave numbers when increasing Co content and the width of peaks became broad. Although cobalt and nickel have extremely similar properties, doped Co or Ni into NiO or CoO can also change the initial status. The shift of Raman peaks position can be attributed to Co doping and the broaden peaks imply more defects or vacancies [46,47]. Doping

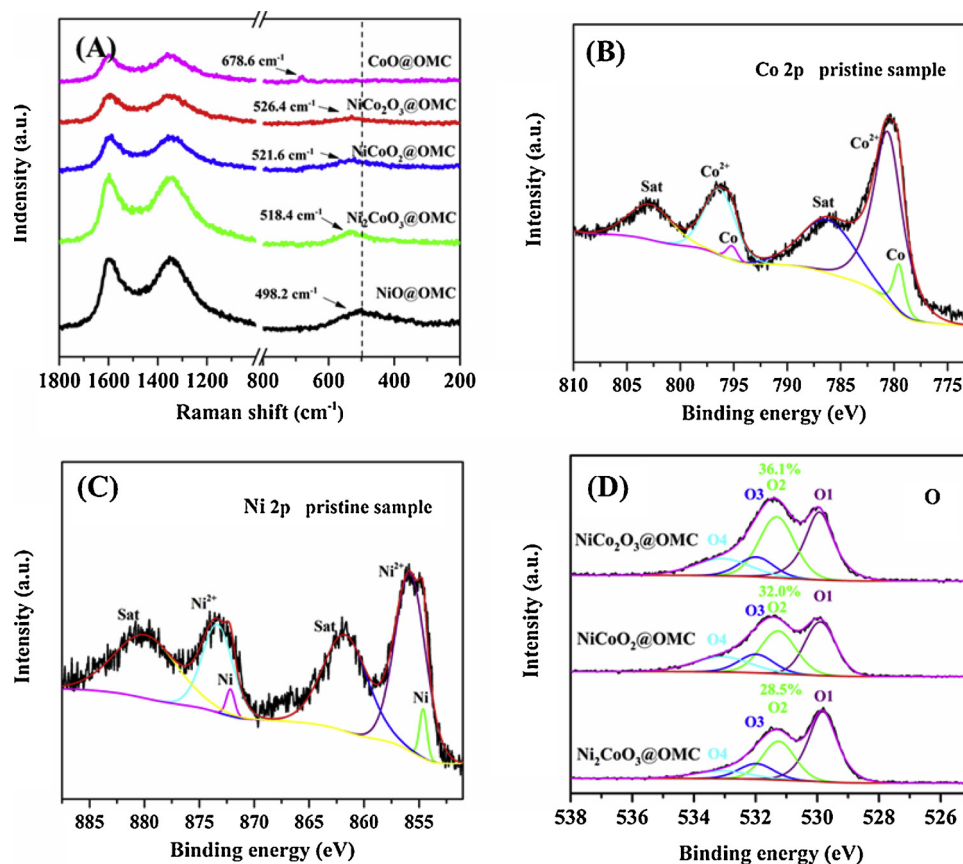


Fig. 3. (A) Raman spectra of the $\text{Ni}_x\text{Co}_y\text{O}_{x+y}@OMC$ composites ($x/y = 1:0, 2:1, 1:1, 1:2, 0:1$). High resolution XPS spectra of the pristine $\text{NiCo}_2\text{O}_3@OMC$ composite: (B) Co 2p photoelectron line, (C) Ni 2p photoelectron line. (D) The O 1s photoelectron lines of $\text{NiCo}_2\text{O}_3@OMC$, $\text{NiCoO}_2@OMC$ and $\text{Ni}_2\text{CoO}_3@OMC$ composites.

of Co or Ni also causes structural changes, which is in a good agreement with the results of XRD measurements.

In order to investigate the surface elemental compositions of the $\text{Ni}_x\text{Co}_y\text{O}_{x+y}@OMC$ composite, the XPS analyses were performed (Fig. 3B–D). The survey spectrum with quantitative information of the $\text{NiCo}_2\text{O}_3@OMC$ is shown in Fig. S3. For the pristine $\text{NiCo}_2\text{O}_3@OMC$ composite (Fig. 3B), the Co 2p spectrum can be deconvoluted into four peaks located at 779.3, 795.1, and 780.5, 796.3 eV, corresponding to Co^0 and Co^{2+} , respectively [48]. Meanwhile, the Ni 2p profiles yield four peaks at 854.2, 872.0 and 855.4, 873.2 eV, which are assigned to Ni^0 and Ni^{2+} , respectively (Fig. 3C). The trace amount of Ni^0 and Co^0 were detected on the surface of pristine $\text{NiCo}_2\text{O}_3@OMC$, which could be attributed to the carbon thermal reduction of OMC. As shown in Fig. 3D, the O 1s spectra of $\text{Ni}_x\text{Co}_y\text{O}_{x+y}@OMC$ ($x/y = 2:1, 1:1, 1:2$) can be deconvoluted into four characteristic peaks, related to the metals-O bond

(529.9 eV for O1), oxygen vacancies or defects (531.3 eV for O2), hydroxyl groups (532.0 eV for O3) and surface adsorbed water molecules (533.1 eV for O4) [49,50]. The characteristic of O1 can be well observed in the three samples, indicating the existence of NiO or CoO. The O2 area ratio of $\text{Ni}_2\text{CoO}_3@OMC$, $\text{NiCoO}_2@OMC$ and $\text{NiCo}_2\text{O}_3@OMC$ was 28.5%, 32.0% and 36.1%, respectively. The largest O2 area ratio of $\text{NiCo}_2\text{O}_3@OMC$ revealed that the $\text{NiCo}_2\text{O}_3@OMC$ possessed more oxygen vacancies than other two samples. Moreover, the concentration of oxygen defects can be increased from 28.5% to 36.1% by decreasing Ni/Co ratio, which is in agreement with the Raman results. This is because Ni-doping into CoO can tune efficiently the electronic density of the adjacent Co atoms, and thus damages the lattice orders after the carbon thermal reduction. Therefore, under the lattice-oxygen-mediated mechanism, the oxygen vacancies on the surface were formed [49,51]. To determine the active surface area of the electrode-

electrolyte interface, electrochemical double-layer capacitances (C_{dl}) were examined by measuring the capacitive currents at different scan rates in the voltage range from -0.05 to 0.05 V. Cyclic voltammetric (CV) measurements were conducted to estimate the effective surface of the OMC and $\text{Ni}_x\text{Co}_y\text{O}_{x+y}@OMC$ composites ($x/y = 2:1, 1:1, 1:2$) in 1 M KOH (Fig. S4). As the scan rate increased from 5 to 400 mV/s, the current densities increased accordingly. It is known that C_{dl} is linearly proportional to the active surface area, which is equivalent to the slope of linear relationship between current density and scan rate [52]. Obviously, the C_{dl} value of $\text{NiCo}_2\text{O}_3@OMC$ (4.05 mF/cm²) was larger than that of $\text{Ni}_2\text{CoO}_3@OMC$ (1 mF/cm²) and $\text{NiCoO}_2@OMC$ (3.4 mF/cm²), indicating that the $\text{NiCo}_2\text{O}_3@OMC$ possesses more exposed active sites and thus better electrocatalytic performance.

3.2. OER catalytic activities of $\text{Ni}_x\text{Co}_y\text{O}_{x+y}@OMC$

Electrocatalytic performance of the OMC and $\text{Ni}_x\text{Co}_y\text{O}_{x+y}@OMC$ composites ($x/y = 2:1, 1:1, 1:2$) towards the OER was investigated by LSV in 1 M KOH (pH = 14) solution in the potential range of 1.1–2.7 V at a scan rate of 5 mV/s. It was clearly seen that the $\text{Ni}_x\text{Co}_y\text{O}_{x+y}@OMC$ ($x/y = 2:1, 1:1, 1:2$) composites exhibited much better catalytic activity compared with the OMC, revealing the overpotentials at the current density of 10 mA/cm² (a metric relevant to comparison of the OER activities) of about 1.8, 2.3 and 3.6 times lower than that of the OMC, respectively (Fig. 4A). The high OER performance of the $\text{Ni}_x\text{Co}_y\text{O}_{x+y}@OMC$ composites can be attributed to the synergistic effect between the rock salt type NiO-CoO and OMC, as well as the oxygen vacancies. Especially, the $\text{NiCo}_2\text{O}_3@OMC$ with the most oxygen vacancies exhibited the lowest overpotential of 281 mV for the OER, which is much lower than the similar catalysts, such as NiCo-NiCoO₂@NC (318 mV) [53] and $\text{NiCoO}_2/\text{CNTs}$ (420 mV) [19] reported so far. Furthermore, the

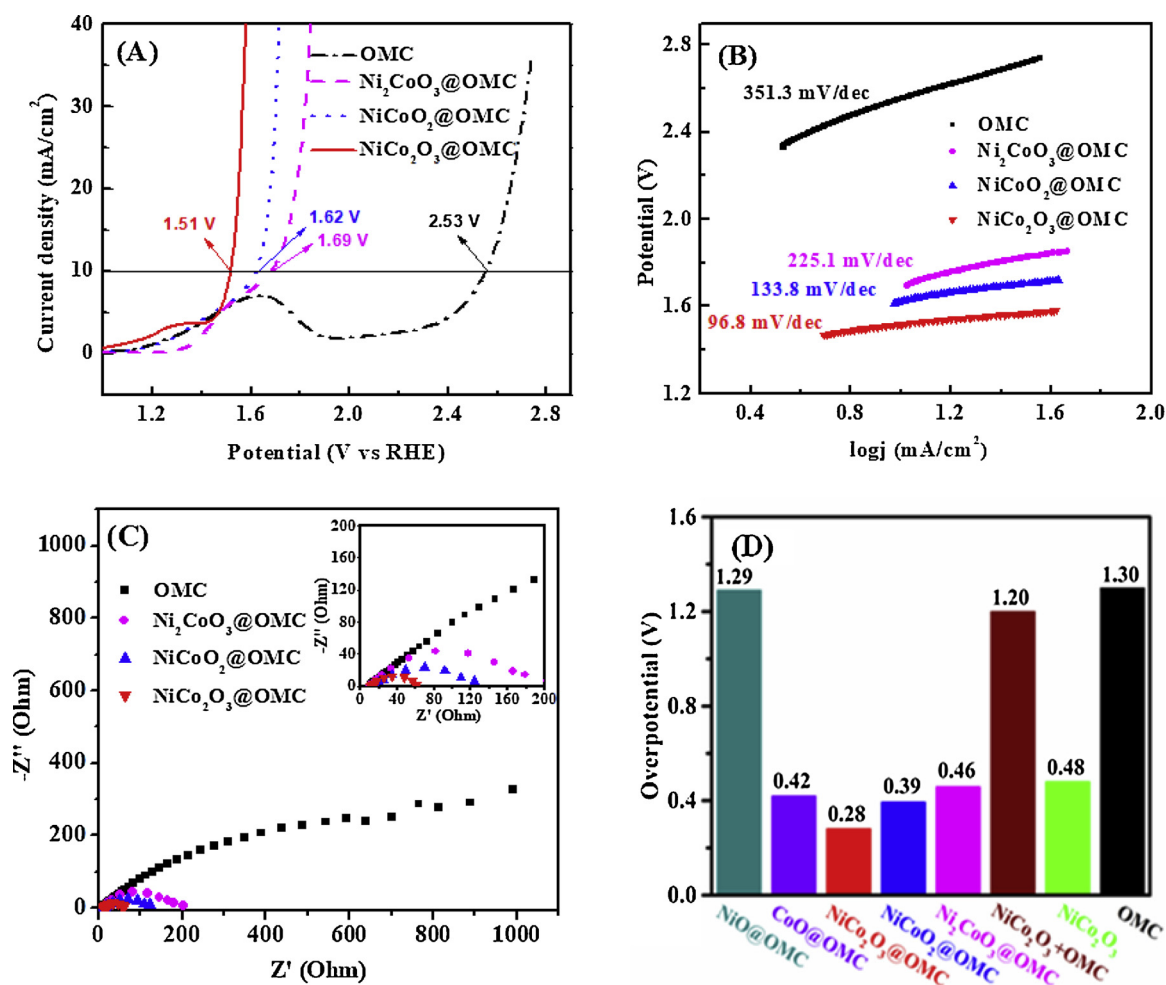


Fig. 4. (A) Polarization curves, (B) the corresponding Tafel plots for the OER, and (C) Nyquist plots obtained at overpotential of 400 mV from the OMC and Ni_xCo_yO_{x+y}@OMC composites (x:y = 2:1, 1:1, 1:2) in 1 M KOH. (D) The overpotential values of all samples.

Table 1

Comparisons of the OER performance for different catalysts.

Catalysts	Electrolyte	Overpotential ^a (mV)	Tafel slope (mV/dec)	Loading amounts (mg/cm ²)	Refs
Co ₃ O ₄ /Co(OH) ₂	1 M KOH	370	103	1.42	[10]
NiCoO ₂ /CNTs ^b	0.1 M KOH	420	156	0.51	[17]
RuO ₂	0.1 M KOH	290	119	0.51	[17]
Ni _x Co _{3-x} O _{4-y}	1 M KOH	320	54	0.36	[26]
Ni _x Co _{1-x} O nanoparticles	0.5 M KOH	350–400	N/A ^c	0.82	[38]
NiCo-NiCoO ₂ @NC ^d	1 M KOH	318	76	0.14	[53]
Ni-Co-OH	1 M NaOH	337	N/A ^c	0.82	[54]
Ni _x Co _{3-x} O ₄ nanowire (Ni/Co = 1:0.3)	1 M NaOH	N/A ^c	54	2.3	[55]
Fe ₃ O ₄ /Co ₃ S ₄	1 M KOH	270	56	0.672	[56]
IrO ₂	1 M KOH	290	71	N/A ^c	[56]
Co@Co ₃ O ₄ /NCs ^e	0.1 M KOH	435	N/A ^c	0.25	[57]
Ni-Co 3D nanosheets	1 M NaOH	340	51	Grown on FTO ^f	[58]
Co ₃ O ₄ UNMs ^g	1 M KOH	307	76	0.32	[59]
NiCo ₂ O ₃ @OMC	1 M KOH	281	96.8	0.567	This work

^a Overpotential vs RHE is measured at current density of 10 mA/cm².

^b CNT, carbon nanotubes.

^c N/A, not available.

^d NC, N-doped carbon.

^e NCs, nitrogen-doped carbon architectures.

^f FTO, fluorinated tin oxide.

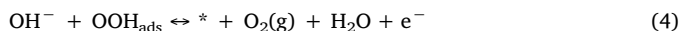
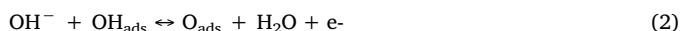
^g UNMs, ultrathin nanomeshes.

overpotential of the NiCo₂O₃@OMC was even slightly lower than that of the RuO₂ (290 mV) [19] and IrO₂ (290 mV) precious catalysts [52] at the same current density (Table 1) [10,19,28,40,53–59].

Oxygen generation rate of the Ni_xCo_yO_{x+y}@OMC nanocomposites was examined by holding the catalyst electrode at 10 mA/cm² for 30 min, and calculated according to the amount of oxygen detected. The oxygen generation rate is determined to be ca. 22.5 μmol/h for the NiCo₂O₃@OMC, ca. 15.3 μmol/h for the NiCoO₂@OMC and ca. 11.6 μmol/h for the Ni₂CoO₃@OMC.

Presently, the overpotentials of at 20 mA/cm² are provided to avoid the influence of the peak at about 1.6 V for Ni-based materials. The corresponding overpotentials of the NiCo₂O₃@OMC, NiCoO₂@OMC and Ni₂CoO₃@OMC are 321, 448 and 551 mV, respectively. The highest OER activity of the NiCo₂O₃@OMC with the highest Co content can be attributed to the highest concentration of oxygen vacancies (36.1%), which can promote the production of low-coordinated Co atoms, enhancing their OH[−] adsorption ability [60]. The oxygen vacancies in the Ni_xCo_yO_{x+y}@OMC composites can not only serve as active sites, but also change the electronic structures of metal oxides, and accordingly guaranteeing the high OER activity [49].

The four reaction steps of common OER mechanism in alkaline electrolyte are shown in Eqs. (1)–(4) as follows [61,62]:



in which * means the surface active site of catalyst, and the OH_{ads}, O_{ads} and OOH_{ads} represent adsorbed intermediates species. Moreover, the OH_{ads} and OOH_{ads} as intermediates in the surface of catalyst interact in a similar way, which limits the performance of catalysts. Here, the binding strength of CoO on the surface of Ni_xCo_yO_{x+y}@OMC is too strong to break, thus the corresponding overpotential results from breaking a bond between the intermediates and the surface through Eq. (3). As for NiO, the binding is too weak, and therefore the overpotential is related to breaking a bond via [Eqs. (1) or (2)] [62]. In general, the relationship between intermediates and catalytic activity of catalyst follows the Sabatier principle [63]. Furthermore, apart from the CoO and NiO, OMC might provide additional active sites for the OER.

Tafel plot (log(j) ~ E) based on the OER mechanism is commonly utilized to assess the catalyst performance for the OER. Likewise, the NiCo₂O₃@OMC yielded a relatively lower Tafel slope of 96.8 mV/dec than those values calculated for the Ni₂CoO₃@OMC (225.1 mV/dec) and NiCoO₂@OMC (133.8 mV/dec) (Fig. 4B). Lower Tafel slope revealed by the NiCo₂O₃@OMC suggests a more favorable kinetic for the OER, relative to the Ni₂CoO₃@OMC and NiCoO₂@OMC. Moreover, the intrinsic activity of catalyst could also be evaluated by the TOF. The TOF values for the various nanocomposites of rock salt type Ni_xCo_yO_{x+y}@OMC (x/y = 0:1, 2:1, 1:1, 1:2, 1:0) were calculated and summarized in Table 2. Apparently, when an overpotential of 281 mV was applied, the NiCo₂O₃@OMC has a TOF value of 0.0341 s^{−1}, which is higher than those values of 0.0213 s^{−1} and 0.0166 s^{−1} for the NiCoO₂@OMC and Ni₂CoO₃@OMC, respectively. Therefore, the high

TOF value of NiCo₂O₃@OMC confirmed its outstanding intrinsic activity as an OER catalyst. For the NiCo₂O₃@OMC, the small amount of Ni atoms could lead to a change in Gibbs free energy (ΔG_{OH}) and the O^{2−} to OH[−] adsorption energy difference (ΔG_O−ΔG_{OH}) at the Co sites, and facilitate the formation of OH[−] and O^{2−} intermediates on Co. Nevertheless, an excess NiO would deteriorate the OER activity, as NiO itself is not an active catalyst for the OER (Fig. S4) [64]. Therefore, an optimal molar ratio of NiO to CoO could effectively promote the OER performance of Ni_xCo_yO_{x+y}@OMC.

Electrochemical impedance spectroscopy (EIS) was performed to further investigate the OER kinetics of the samples. Typical Nyquist plots with well-defined semicircles were acquired (Fig. 4C). The corresponding charge transfer resistance (R_{ct}) values of the OMC and Ni_xCo_yO_{x+y}@OMC composites (x/y = 2:1, 1:1, 1:2) were 1470, 231, 179 and 50 Ohm, respectively (Fig. 4C and Table S3). The above results were in a good accordance with the tendency of LSV measurements and Tafel slopes, indicating better charge transfer kinetics of the NiCo₂O₃@OMC. The enhanced activity can be ascribed to the uniform distribution of the metal oxides on the conducting OMC, owing to more exposed active sites for the penetration of the electrolyte and accelerating the reaction kinetics. Moreover, the well-defined porosity of the NiCo₂O₃@OMC contributes to the enhanced activity due to the effective charge and mass transport within the electrodes. The superior OER performance of the NiCo₂O₃@OMC may be explained as follows. The optimized molar ratio of NiO and CoO is crucial for the interaction between metal element and O-containing species in the oxygen electrocatalytic process. The NiCo₂O₃@OMC possesses more oxygen vacancies, which can significantly enhance reactivity and the number of surface active sites. Doping of Co or Ni also causes structural changes and produces more defects, promoting the electrocatalytic performance of the OER [42,49]. The ultrasmall size of the Ni_xCo_yO_{x+y} nanoparticles provides shortened charge transport pathways and a greatly increased surface area, which favors the interfacial charge transfer, providing high electrocatalytic activity.

For comparison, the mixture of the OMC and NiCo₂O₃ (denoted as NiCo₂O₃+OMC) with the same mass ratio as that of the as-developed rock salt type NiCo₂O₃@OMC was prepared. The electrocatalytic performances of NiCo₂O₃, NiCo₂O₃+OMC, NiO@OMC and CoO@OMC for the OER was also tested (Fig. S5A and S5C) and the overpotential values of all the samples are exhibited in Fig. 4D. The overpotential of the NiCo₂O₃ (480 mV) and NiCo₂O₃+OMC (1200 mV) was significantly higher than that of the NiCo₂O₃@OMC (281 mV), confirming that the addition of OMC to the NiCo₂O₃ decreased the OER activity of the mixture by reducing the effective composition of catalyst. In particular, the OMC support of the NiCo₂O₃@OMC has been widely used not only to promote electron transfer but also to serve as complementary sites for the OER, thereby enhancing the ability of the materials to electrocatalyze the OER [65]. In addition, the overpotentials of the NiO@OMC (1290 mV) and CoO@OMC (420 mV) were also significantly higher than that of the NiCo₂O₃@OMC. This is because both the Ni and Co species can interact with water to form M–O (M = Ni or Co) bonds and accordingly facilitate water splitting. The LSV results also indicate that the presence of Co facilitates the oxidation of Ni²⁺ to Ni³⁺ at relatively lower potentials. In other words, it is noted a cathodic shift of the Ni²⁺/Ni³⁺ redox features in the presence of Co [66]. Furthermore, the OMC not only acts as a buffer to prevent the aggregation of the ultrasmall Ni_xCo_yO_{x+y} nanoparticles during the catalytic process, leading to a high electrocatalytic stability. Moreover, the Ni_xCo_yO_{x+y} nanoparticles in situ confined in the OMC matrix are more conductive than those electrodes prepared by a physical mixing of the Ni_xCo_yO_{x+y} particles and OMC (i.e., Ni_xCo_yO_{x+y}+OMC). This result demonstrated that the rock salt type Ni_xCo_yO_{x+y}@OMC catalysts have high catalytic activity and stability, which can be attributed to the synergetic effect between Ni_xCo_yO_{x+y} and OMC.

Moreover, the typical Nyquist plots of the NiCo₂O₃, NiCo₂O₃+OMC and NiCo₂O₃@OMC are shown in Fig. S5B and the derived R_{ct} values

Table 2
Comparison of the TOF values of the different OER catalysts.

Catalysts	Current density at overpotential of 281 mV (mA/cm ²)	TOF (s ^{−1})
NiCo ₂ O ₃ @OMC	10.00	0.0341
NiCoO ₂ @OMC	6.24	0.0213
Ni ₂ CoO ₃ @OMC	6.13	0.0166
CoO@OMC	4.84	0.0037
NiO@OMC	5.11	0.0038

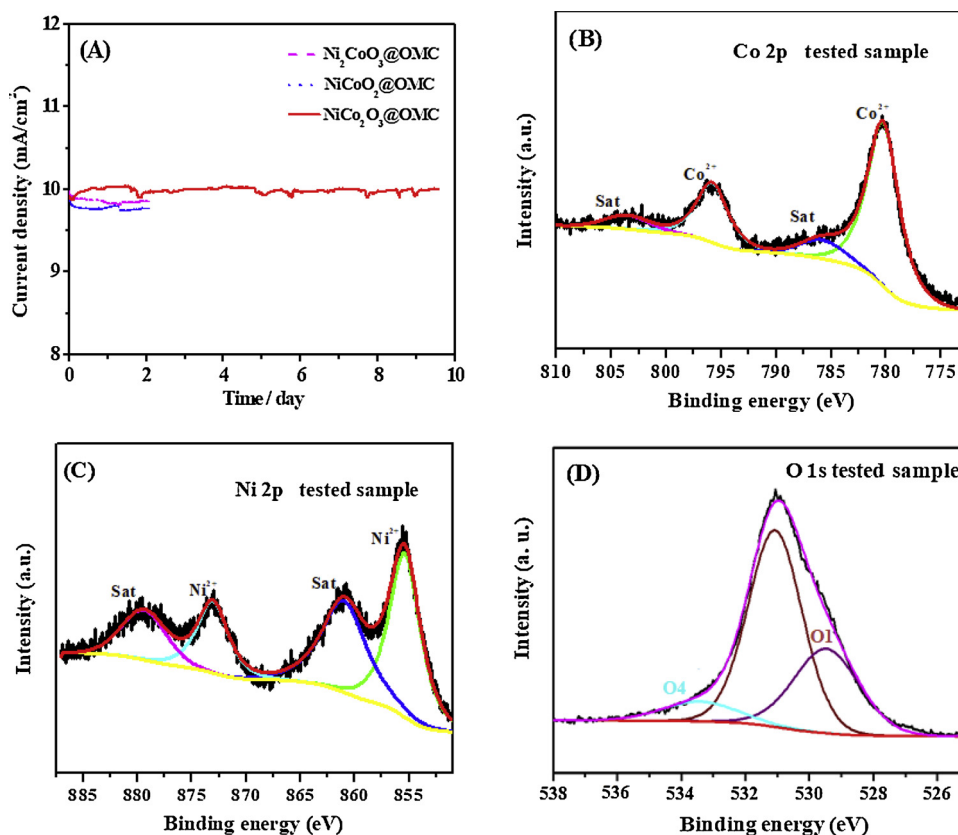


Fig. 5. (A) Stability tests performed at 1.51, 1.62 and 1.69 V (vs. RHE) for the $\text{NiCo}_2\text{O}_3@\text{OMC}$, $\text{NiCoO}_2@\text{OMC}$ and $\text{Ni}_2\text{CoO}_3@\text{OMC}$, respectively. High resolution XPS spectra of the $\text{NiCo}_2\text{O}_3@\text{OMC}$ composite after testing at OER condition: (B) Co 2p photoelectron line, (C) Ni 2p photoelectron line, and (D) O 1s photoelectron line.

are summarized in Table S3. It is noted that $\text{NiCo}_2\text{O}_3@\text{OMC}$ exhibited a lower R_{ct} value than those of the NiCo_2O_3 and $\text{NiCo}_2\text{O}_3 + \text{OMC}$. The lowest R_{ct} value of the $\text{NiCo}_2\text{O}_3@\text{OMC}$ may be ascribed to its unique hybrid nanostructure, in which the pore structure of the OMC can accommodate and anchor the ultrasmall Ni-Co oxides nanoparticles, resulting in a faster charge transfer at the interface between the NiCo_2O_3 nanoparticles and the ordered mesoporous channels of the OMC. Furthermore, the high conductivity of OMC contributes to the enhanced activity of the $\text{NiCo}_2\text{O}_3@\text{OMC}$ by assuring effective charge transfer and mass transport within the electrode.

To gain an insight into the high OER catalytic activity observed for the $\text{NiCo}_2\text{O}_3@\text{OMC}$, we also used the same procedure to synthesize $\text{Ni}_x\text{Co}_y\text{O}_{x+y}$ samples ($x:y = 1:0, 1:2, 0:1$) without the OMC nanoreactor. The phases of the $\text{Ni}_x\text{Co}_y\text{O}_{x+y}$ samples ($x:y = 1:0, 1:2, 0:1$) are NiO, NiCo_2O_3 and CoO respectively. Apart from the NiO, the other samples can not form single rock salt structure after reacting at 350 °C for 2 h in the absence of the OMC support. As reported previously, the crystal phases of cobalt nitrate and nickel nitrate after calcination depend on the calcination temperature, atmosphere and reduction time [46,67]. Therefore, we can deduce that the OMC can be used to fabricate the low valent state of ultrasmall-sized NiO and CoO nanoparticles at low temperatures.

Long-term durability is another key criterion in the selection of electrocatalysts. To examine the stability of the $\text{Ni}_x\text{Co}_y\text{O}_{x+y}@\text{OMC}$ nanocomposites for the OER in alkaline solution, CA was carried out at a corresponding current density of 10 mA/cm^2 . As shown in Fig. 5A, the $\text{NiCo}_2\text{O}_3@\text{OMC}$ reveals a negligible change in the current density after a continuous electrolysis for more than 230 h, implying a very good electrochemical stability for this electrocatalyst. In contrast, the current density dropped significantly after 50 h for the $\text{Ni}_2\text{CoO}_3@\text{OMC}$ and $\text{NiCoO}_2@\text{OMC}$ catalysts, and thus the electrochemical stability test experiments were terminated for the two

catalysts. The fluctuation phenomenon appeared in the curves is mainly attributed to the generation of O_2 during the test process. More importantly, the $\text{NiCo}_2\text{O}_3@\text{OMC}$ has exhibited a comparable durability to the catalyst reported in literature [68]. The stability test results also indicated that the $\text{NiCo}_2\text{O}_3@\text{OMC}$ catalyst maintained the highest chemical stability among the $\text{Ni}_x\text{Co}_y\text{O}_{x+y}@\text{OMC}$ catalysts for the OER, which is probably mainly attributed to the relatively low corrosion rate in the defective conducting channels [69]. In such a hybrid $\text{NiCo}_2\text{O}_3@\text{OMC}$ composite, the ultrasmall Ni-Co double oxides nanoparticles were partially embedded into the ordered mesoporous channels of the OMC, which not only provide a shorter diffusion length for mass transport, but also a confined space to prevent the agglomeration and shedding of the nanoparticles, resulting in a significantly enhanced stability.

After the stability test, XPS analysis was conducted, and the XPS spectra of the $\text{NiCo}_2\text{O}_3@\text{OMC}$ catalyst are displayed in Fig. 5B-D and S6. As shown in Fig. S6, no obvious change in the Ni/Co ratio was observed, indicating a good stability of the $\text{NiCo}_2\text{O}_3@\text{OMC}$. The peaks of Co^0 and Ni^0 were disappeared, suggesting that the Co^0 and Ni^0 on the catalyst surface have transformed to Co^{2+} and Ni^{2+} [70]. The presence of Ni^{2+} and Co^{2+} synergistic with the OMC promotes the electrocatalytic activity for the OER. Moreover, the O 1s spectrum of the $\text{NiCo}_2\text{O}_3@\text{OMC}$ can be deconvoluted into three characteristic peaks, especially the peak located at ~531 eV increased significantly, nevertheless it does not mean an increase of oxygen vacancies. This peak is also related to OH species, corresponding to the formation of OOH_{ads} during the OER process [71].

4. Conclusions

In summary, we developed a general strategy to synthesize rock salt type nanocomposites of Ni-Co oxides with different Ni/Co molar ratios supported on ordered mesoporous carbon (i.e., $\text{Ni}_x\text{Co}_y\text{O}_{x+y}@\text{OMC}$, $x/$

$y = 2:1, 1:1, 1:2$). When explored as an electrocatalyst for the OER, the $\text{NiCo}_2\text{O}_3\text{@OMC}$ composite exhibited a superior OER activity and high stability in an alkaline solution. The outstanding performance can be mainly attributed to the intrinsic activity of rock salt type $\text{NiCo}_2\text{O}_3\text{@OMC}$, confirmed by its high turnover frequency value. Additional contribution probably originates from the nickel and cobalt oxides which possess abundant active sites and oxygen vacancies, high conductivity of the OMC, and the synergistic effect of the ultrasmall oxides and merits of the OMC. Therefore, the as-developed noble metal-free rock salt type $\text{NiCo}_2\text{O}_3\text{@OMC}$ catalyst is highly electroactive and cost-effective and very promising for OER-related applications in a large scale.

Acknowledgements

This work was financially supported by National Natural Science Foundation of China (81673172, 21475144, 51502036), Major Program of Shandong Province Natural Science Foundation (ZR2018ZC0125), Natural Science Foundation of Distinguished Young Scholars for Fujian Province (2019J06015) and China Postdoctoral Science Foundation funded project (2019M652325).

Appendix A. Supplementary data

Supplementary material related to this article can be found, in the online version, at doi:<https://doi.org/10.1016/j.apcatb.2019.117852>.

References

- J. Zhang, Z. Zhao, Z. Xia, A metal-free bifunctional electrocatalyst for oxygen reduction and oxygen evolution reactions, *Nat. Nanotechnol.* 10 (2015) 444–452, <https://doi.org/10.1038/nnano.2015.48>.
- I.S. Amiinu, X. Liu, Z. Pu, W. Li, Q. Li, J. Zhang, H. Tang, H. Zhang, S. Mu, From 3D ZIF nanocrystals to $\text{Co-N}_x\text{/C}$ nanorod array electrocatalysts for ORR, OER, and Zn-air batteries, *Adv. Funct. Mater.* 28 (2018) 1704638, <https://doi.org/10.1002/adfm.201704638>.
- P. Chen, K. Xu, T. Zhou, Y. Tong, J. Wu, H. Cheng, X. Lu, H. Ding, C. Wu, Y. Xie, Strong-coupled cobalt borate nanosheets/graphene hybrid as electrocatalyst for water oxidation under both alkaline and neutral conditions, *Angew. Chem. Int. Ed.* 55 (2016) 2488–2492, <https://doi.org/10.1002/anie.201511032>.
- I.S. Amiinu, Z. Pu, X. Liu, K.A. Owusu, H.G.R. Monestel, F.O. Boakye, H. Zhang, S. Mu, Multifunctional $\text{Mo-N/C}@ \text{MoS}_2$ electrocatalysts for HER, OER, ORR, and Zn-air batteries, *Adv. Funct. Mater.* 27 (2017) 1702300, <https://doi.org/10.1002/adfm.201702300>.
- Y. Wang, B. Fang, X. Wang, A. Ignaszak, Y. Liu, A. Li, L. Zhang, J. Zhang, Recent advancements in the development of bifunctional electrocatalysts for oxygen electrodes in unitized regenerative fuel cells (URFCs), *Prog. Mater. Sci.* 98 (2018) 108–167, <https://doi.org/10.1016/j.pmatsci.2018.06.001>.
- Z. Wu, B. Fang, Z. Wang, C. Wang, Z. Liu, F. Liu, W. Wang, A. Alfantazi, D. Wang, D. Wilkinson, MoS_2 nanosheets: a designed structure with high active site density for the hydrogen evolution reaction, *ACS Catal.* 3 (2013) 2101–2107, <https://doi.org/10.1021/cs400384h>.
- G.C. da Silva, N. Perini, E.A. Ticianelli, Effect of temperature on the activities and stabilities of hydrothermally prepared IrO_x nanocatalyst layers for the oxygen evolution reaction, *Appl. Catal. B: Environ.* 218 (2017) 287–297, <https://doi.org/10.1016/j.apcatb.2017.06.044>.
- Z. Wu, C. Tang, P. Zhou, Z. Liu, Y. Xu, D. Wang, B. Fang, Enhanced hydrogen evolution catalysis from osmotically swollen ammoniated MoS_2 , *J. Mater. Chem. A* 3 (2015) 13050–13056, <https://doi.org/10.1039/C5TA02010G>.
- Z. Pu, I.S. Amiinu, Z. Kou, W. Li, S. Mu, RuP_2 -based catalysts with platinum-like activity and higher durability for the hydrogen evolution reaction at all pH values, *Angew. Chem. Int. Ed.* 56 (2017) 11559–11564, <https://doi.org/10.1002/anie.201704911>.
- S.V. Devaguptapu, S. Hwang, S. Karakalos, S. Zhao, S. Gupta, D. Su, H. Xu, G. Wu, Morphology control of carbon-free spinel NiCo_2O_4 catalysts for enhanced bifunctional oxygen reduction and evolution in alkaline media, *ACS Appl. Mater. Interfaces* 9 (2017) 44567–44578, <https://doi.org/10.1021/acsami.7b16389>.
- Y. Zhang, Y. Wang, C. Han, S. Jia, S. Zhou, J. Zhang, Tungsten-coated nano-boron carbide as a non-noble metal bifunctional electrocatalyst for oxygen evolution and hydrogen evolution reactions in alkaline media, *Nanoscale* 9 (2017) 19176–19182, <https://doi.org/10.1039/C7NR08092A>.
- P. Wang, Z. Pu, Y. Li, L. Wu, Z. Tu, M. Jiang, Z. Kou, I.S. Amiinu, S. Mu, Iron-doped nickel phosphide nanosheet arrays: an efficient bifunctional electrocatalyst for water splitting, *ACS Appl. Mater. Interfaces* 9 (2017) 26001–26007, <https://doi.org/10.1021/acsami.7b06305>.
- W. Zhong, Z. Lin, S. Feng, D. Wang, S. Shen, Q. Zhang, L. Gu, Z. Wang, B. Fang, Improved oxygen evolution activity of IrO_2 by in situ engineering of ultra-small Ir sphere shell utilizing pulse laser, *Nanoscale* 11 (2019) 4407–4413, <https://doi.org/10.1039/C8NR10163A>.
- X. Zhao, X. Li, Y. Yan, Y. Xing, S. Lu, L. Zhao, S. Zhou, Z. Peng, J. Zeng, Electrical and structural engineering of cobalt selenide nanosheets by Mn modulation for efficient oxygen evolution, *Appl. Catal. B: Environ.* 236 (2018) 569–575, <https://doi.org/10.1016/j.apcatb.2018.05.054>.
- T. Li, Y. Lv, J. Su, Y. Wang, Q. Yang, Y. Zhang, J. Zhou, L. Xu, D. Sun, Y. Tang, Anchoring CoFe_2O_4 nanoparticles on N-doped carbon nanofibers for high-performance oxygen evolution reaction, *Adv. Sci.* 4 (2017) 1700226, <https://doi.org/10.1002/advs.201700226>.
- X. Li, J. Wei, Q. Li, S. Zheng, Y. Xu, P. Du, C. Chen, J. Zhao, H. Xue, Q. Xu, H. Pang, Nitrogen-doped cobalt oxide nanostructures derived from cobalt-alanine complexes for high-performance oxygen evolution reactions, *Adv. Funct. Mater.* 28 (2018) 1800886, <https://doi.org/10.1002/adfm.201800886>.
- L. Ma, H. Zhou, Y. Sun, S. Xin, C. Xiao, A. Kumtani, T. Matsue, P. Zhang, S. Ding, F. Li, Nanosheet-structured NiCo_2O_4 /carbon nanotubes hybrid composite as a novel bifunctional oxygen electrocatalyst, *Electrochim. Acta* 252 (2017) 338–349, <https://doi.org/10.1016/j.electacta.2017.08.192>.
- X. Zhou, Z. Liu, Y. Wang, Y. Ding, Facet effect of Co_3O_4 nanocrystals on visible-light driven water oxidation, *Appl. Catal. B: Environ.* 237 (2018) 74–84, <https://doi.org/10.1016/j.apcatb.2018.05.067>.
- Y.-J. Li, L. Cui, P.-F. Da, K.-W. Qiu, W.-J. Qin, W.-B. Hu, X.-W. Du, K. Davey, T. Ling, S.-Z. Qiao, Multiscale structural engineering of Ni-Doped CoO nanosheets for zinc-air batteries with high power density, *Adv. Mater.* 30 (2018) 1804653, <https://doi.org/10.1002/adma.201804653>.
- J. Wu, Z. Ren, S. Du, L. Kong, B. Liu, W. Xi, J. Zhu, H. Fu, A highly active oxygen evolution electrocatalyst: ultrathin CoNi double hydroxide/ CoO nanosheets synthesized via interface-directed assembly, *Nano Res.* 9 (2016) 713–725, <https://doi.org/10.1007/s12274-015-0950-4>.
- Y. Ma, X. Dai, M. Liu, J. Yong, H. Qiao, A. Jin, Z. Li, X. Huang, H. Wang, X. Zhang, Strongly coupled FeNi alloys/ NiFe_2O_4 /carbonitride layers-assembled microboxes for enhanced oxygen evolution reaction, *ACS Appl. Mater. Interfaces* 8 (2016) 34396–34404, <https://doi.org/10.1021/acsami.6b11821>.
- R.P. Antony, A.K. Satpati, K. Bhattacharyya, B.N. Jagatap, MOF derived non-stoichiometric $\text{Ni}_x\text{Co}_{3-x}\text{O}_{4-y}$ nanocage for superior electrocatalytic oxygen evolution, *Adv. Mater. Interfaces* 3 (2016) 1600632, <https://doi.org/10.1002/admi.201600632>.
- V. Skvortsova, N. Mironova-Ulman, A. Kuzmin, U. Ulmanis, Growth and optical properties of transition metal oxides single crystal solid solutions, *J. Alloys Compd.* 442 (2007) 328–330, <https://doi.org/10.1016/j.jallcom.2006.09.165>.
- D. He, H. Tang, Z. Kou, M. Pan, X. Sun, J. Zhang, S. Mu, Engineered graphene materials: synthesis and applications for polymer electrolyte membrane fuel cells, *Adv. Mater.* 29 (2017) 1601741, <https://doi.org/10.1002/adma.201601741>.
- He, D.Z. Kou, Y. Xiong, K. Cheng, X. Chen, M. Pan, S. Mu, Simultaneous sulfonation and reduction of graphene oxide as highly efficient supports for metal nanocatalysts, *Carbon* 66 (2014) 312–319, <https://doi.org/10.1016/j.carbon.2013.09.005>.
- H. Zhang, H. Qiao, H. Wang, N. Zhou, J. Chen, Y. Tang, J. Li, C. Huang, Nickel cobalt oxide/carbon nanotubes hybrid as a high-performance electrocatalyst for metal/air battery, *Nanoscale* 6 (2014) 10235–10242, <https://doi.org/10.1039/C4NR02125H>.
- A. Eftekhari, B. Fang, Electrochemical hydrogen storage: opportunities for fuel storage, batteries, fuel cells, and supercapacitors, *Int. J. Hydrogen Energy* 42 (2017) 25143–25165, <https://doi.org/10.1016/j.ijhydene.2017.08.103>.
- C. Xiao, Y. Li, X. Lu, C. Zhao, Bifunctional porous $\text{NiFe/NiCo}_2\text{O}_4\text{/Ni}$ foam electrodes with triple hierarchy and double synergies for efficient whole cell water splitting, *Adv. Funct. Mater.* 26 (2016) 3515–3523, <https://doi.org/10.1002/adfm.201505302>.
- X.F. Lu, L.F. Gu, J.W. Wang, J.X. Wu, P.Q. Liao, G.R. Li, Bimetal-organic framework derived $\text{CoFe}_2\text{O}_4\text{/C}$ porous hybrid nanorod arrays as high-performance electrocatalysts for oxygen evolution reaction, *Adv. Mater.* 29 (2017) 1604437, <https://doi.org/10.1002/adma.201604437>.
- T. Börner, S. Rämisch, E.R. Reddem, S. Bartsch, A. Vogel, A.-M.W.H. Thunnissen, P. Adlercreutz, C. Grey, Explaining operational instability of amine transaminases: substrate-induced inactivation mechanism and influence of quaternary structure on enzyme-cofactor intermediate stability, *ACS Catal.* 7 (2017) 1259–1269, <https://doi.org/10.1021/acscatal.6b02100>.
- H. Osgood, S.V. Devaguptapu, H. Xu, J. Cho, G. Wu, Transition metal (Fe, Co, Ni, and Mn) oxides for oxygen reduction and evolution bifunctional catalysts in alkaline media, *Nano Today* 11 (2016) 601–625, <https://doi.org/10.1016/j.nantod.2016.09.001>.
- J.X. Feng, S.H. Ye, H. Xu, Y.X. Tong, G.R. Li, Design and synthesis of FeOOH/CeO_2 heterolayered nanotube electrocatalysts for the oxygen evolution reaction, *Adv. Mater.* 28 (2016) 4698–4703, <https://doi.org/10.1002/adma.201600054>.
- Y.R. Zheng, M.R. Gao, Q. Gao, H.H. Li, J. Xu, Z.Y. Wu, S.H. Yu, An efficient $\text{CeO}_2\text{/CoSe}_2$ nanobelt composite for electrochemical water oxidation, *Small* 11 (2015) 182–188, <https://doi.org/10.1002/smll.201401423>.
- L. Zeng, Q. Li, D. Tang, G. Chen, M. Wei, Metal platinum-wrapped mesoporous carbon for sensitive electrochemical immunosensing based on cyclodextrin functionalized graphene nanosheets, *Electrochim. Acta* 68 (2012) 158–165, <https://doi.org/10.1016/j.electacta.2012.02.045>.
- D. Tang, J. Tang, Q. Li, B. Su, G. Chen, Ultrasensitive aptamer-based multiplexed electrochemical detection by coupling distinguishable signal tags with catalytic recycling of DNase I, *Anal. Chem.* 83 (2011) 7255–7259, <https://doi.org/10.1021/ac201891w>.
- M. Kim, S. Kim, D. Song, S. Oh, K.J. Chang, E. Cho, Promotion of electrochemical oxygen evolution reaction by chemical coupling of cobalt tomolybdenum carbide,

- Appl. Catal. B: Environ. 227 (2018) 340–348, <https://doi.org/10.1016/j.apcatb.2018.01.051>.
- [37] Z.-F. Huang, J. Wang, Y. Peng, C.-Y. Jung, A. Fisher, X. Wang, Design of efficient bifunctional oxygen reduction/evolution electrocatalyst: recent advances and perspectives, *Adv. Energy Mater.* 7 (2017) 1700544, <https://doi.org/10.1002/aenm.201700544>.
- [38] K. Fominykh, G.C. Tok, P. Zeller, H. Hajjiyani, T. Miller, M. Döblinger, R. Pentcheva, T. Bein, D. Fattakhova-Rohlfing, Rock salt Ni/Co oxides with unusual nanoscale-stabilized composition as water splitting electrocatalysts, *Adv. Funct. Mater.* 27 (2017) 1605121, <https://doi.org/10.1002/adfm.201605121>.
- [39] L. Yan, H. Ren, Y. Guo, G. Wang, C. Liu, Y. Wang, X. Liu, L. Zeng, A. Liu, Rock salt type NiO assembled on ordered mesoporous carbon as peroxidase mimetic for colorimetric assay of gallic acid, *Talanta* 201 (2019) 406–412, <https://doi.org/10.1016/j.talanta.2019.04.025>.
- [40] Y. Guo, L. Yan, R. Zhang, H. Ren, A. Liu, CoO-supported ordered mesoporous carbon nanocomposite based nanozyme with peroxidase-like activity for colorimetric detection of glucose, *Process Biochem.* 81 (2019) 92–98, <https://doi.org/10.1016/j.procbio.2019.03.005>.
- [41] T.M. Roffi, K. Uchida, S. Nozaki, Structural, electrical, and optical properties of $\text{Co}_3\text{Ni}_{1-x}\text{O}$ films grown by metalorganic chemical vapor deposition, *J. Cryst. Growth* 414 (2015) 123–129, <https://doi.org/10.1016/j.jcrysgro.2014.10.027>.
- [42] Y. Zhang, J. Zang, L. Dong, X. Cheng, Y. Zhao, Y. Wang, A Ti-coated nano-SiC supported platinum electrocatalyst for improved activity and durability in direct methanol fuel cells, *J. Mater. Chem. A* 2 (2014) 10146–10153, <https://doi.org/10.1039/C4TA00618F>.
- [43] L.X. Zeng, X. Chen, R.P. Liu, L.X. Lin, C. Zheng, L.H. Xu, F.Q. Luo, Q.R. Qian, Q.H. Chen, M.D. Wei, Green synthesis of a Se/HPCF-rGO composite for Li-Se batteries with excellent long-term cycling performance, *J. Mater. Chem. A* 5 (2017) 22997–23005, <https://doi.org/10.1039/C7TA06884K>.
- [44] L. Zeng, X. Huang, X. Chen, C. Zheng, Q. Qian, Q. Chen, M. Wei, Ge/GeO₂-ordered mesoporous carbon nanocomposite for rechargeable lithium-ion batteries with a long-term cycling performance, *ACS Appl. Mater. Interfaces* 8 (2016) 232–239, <https://doi.org/10.1021/acsami.5b08470>.
- [45] S.H. Lee, H.M. Cheong, N.G. Park, C.E. Tracy, A. Mascarenhas, D.K. Benson, S.K. Deb, Raman spectroscopic studies of Ni-W oxide thin films, *Solid State Ion.* 140 (2001) 135–139, [https://doi.org/10.1016/S0167-2738\(01\)00707-X](https://doi.org/10.1016/S0167-2738(01)00707-X).
- [46] Z.Y. Hou, T. Yashima, Supported Co catalysts for methane reforming with CO₂, *React. Kinet. Catal. Lett.* 81 (2004) 153–159, <https://doi.org/10.1023/B:REAC.0000016529.84565.e5>.
- [47] Z.H. Wang, H. Zhou, D.M. Han, F.B. Gu, Electron compensation in P-Type 3DOM NiO by Sn doping for enhanced formaldehyde sensing performance, *J. Mater. Chem. C* 5 (2017) 3254–3263, <https://doi.org/10.1039/C7TC00226B>.
- [48] X. Liu, W. Liu, M. Ko, M. Park, M.G. Kim, P. Oh, S. Chae, S. Park, A. Casimir, G. Wu, J. Cho, Metal (Ni, Co)-metal oxides/graphene nanocomposites as multifunctional electrocatalysts, *Adv. Funct. Mater.* 25 (2015) 5799–5808, <https://doi.org/10.1002/adfm.201502217>.
- [49] Y. Wang, C. Xie, Z. Zhang, D. Liu, R. Chen, S. Wang, In situ exfoliated, N-doped, and edge-rich ultrathin layered double hydroxides nanosheets for oxygen evolution reaction, *Adv. Funct. Mater.* 28 (2018) 1703363, <https://doi.org/10.1002/adfm.201703363>.
- [50] Y. Zhang, Y. Wang, S. Jia, H. Xu, J. Zang, J. Lu, X. Xu, A hybrid of NiMo-Mo₂C/C as non-noble metal electrocatalyst for hydrogen evolution reaction in an acidic solution, *Electrochim. Acta* 222 (2016) 747–754, <https://doi.org/10.1016/j.electacta.2016.11.031>.
- [51] Y. Zhou, S. Sun, J. Song, S. Xi, B. Chen, Y. Du, A.C. Fisher, F. Cheng, X. Wang, H. Zhang, Z.J. Xu, Enlarged Co-O covalency in octahedral sites leading to highly efficient spinel oxides for oxygen evolution reaction, *Adv. Mater.* 32 (2018) 1802912, <https://doi.org/10.1002/adma.201802912>.
- [52] X. Wang, R. Liu, Y. Zhang, L. Zeng, A. Liu, Hierarchical Ni₃S₂-NiOOH hetero-nanocomposite grown on nickel foam as a noble-metal-free electrocatalyst for hydrogen evolution reaction in alkaline electrolyte, *Appl. Surf. Sci.* 456 (2018) 164–173, <https://doi.org/10.1016/j.apsusc.2018.06.107>.
- [53] Y. Xiao, P. Zhang, X. Zhang, X. Dai, Y. Ma, Y. Wang, Y. Jiang, M. Liu, Y. Wang, Bimetallic thin film NiCo-NiCoO₂/NC as a superior bifunctional electrocatalyst for overall water splitting in alkaline media, *J. Mater. Chem. A* 5 (2017) 15901–15912, <https://doi.org/10.1039/C7TA03629A>.
- [54] J. Du, T. Zhang, J. Xing, C. Xu, Hierarchical porous Fe₃O₄/Co₃S₄ nanosheets as an efficient electrocatalyst for the oxygen evolution reaction, *J. Mater. Chem. A* 5 (2017) 9210–9216, <https://doi.org/10.1039/C7TA02108A>.
- [55] L. Li, T. Tian, J. Jiang, L. Ai, Hierarchically porous Co₃O₄ architectures with honeycomb-like structures for efficient oxygen generation from electrochemical water splitting, *J. Power Sources* 294 (2015) 103–111, <https://doi.org/10.1016/j.jpowsour.2015.06.056>.
- [56] H. Zhu, D. Yu, S. Zhang, J. Chen, W. Wu, M. Wan, L. Wang, M. Zhang, M. Du, Morphology and structure engineering in nanofiber reactor: tubular hierarchical integrated networks composed of dual phase octahedral CoMn₂O₄/carbon nanofibers for water oxidation, *Small* 13 (2017) 17000468, <https://doi.org/10.1002/smll.201700468>.
- [57] C. Qi, L. Zhang, G. Xu, Z. Sun, A. Zhao, D. Jia, Co@Co₃O₄ nanoparticle embedded nitrogen-doped carbon architectures as efficient bicatalysts for oxygen reduction and evolution reactions, *Appl. Surf. Sci.* 427 (2018) 319–327, <https://doi.org/10.1016/j.apsusc.2017.08.209>.
- [58] A. Aijaz, J. Masa, C. Rosler, W. Xia, P. Weide, A.J. Botz, R.A. Fischer, W. Schuhmann, M. Muhler, Co@Co₃O₄ encapsulated in carbon nanotube-grafted nitrogen-doped carbon polyhedra as an advanced bifunctional oxygen electrode, *Angew. Chem. Int. Ed.* 55 (2016) 4087–4091, <https://doi.org/10.1002/anie.201509382>.
- [59] Y. Li, F.-M. Li, X.-Y. Meng, S.-N. Li, J.-H. Zeng, Y. Chen, Ultrathin Co₃O₄ nanosheets for the oxygen evolution reaction, *ACS Catal.* 8 (2018) 1913–1920, <https://doi.org/10.1021/acscatal.7b03949>.
- [60] L. Zhuang, Y. Jia, T. He, A. Du, X. Yan, L. Ge, Z. Zhu, X. Yao, Tuning oxygen vacancies in two-dimensional iron-cobalt oxide nanosheets through hydrogenation for enhanced oxygen evolution activity, *Nano Res.* 11 (2018) 3509–3515, <https://doi.org/10.1007/s12274-018-2050-8>.
- [61] V. Vij, S. Sultan, A.M. Harzandi, A. Meena, J.N. Tiwari, W.G. Lee, T. Yoon, K.S. Kim, Nickel-based electrocatalysts for energy-related applications: oxygen reduction, oxygen evolution, and hydrogen evolution reactions, *ACS Catal.* 7 (2017) 7196–7225, <https://doi.org/10.1021/acscatal.7b01800>.
- [62] R. Frydendal, M. Busch, N.B. Halck, E.A. Paoli, P. Krtil, I. Chorkendorff, J. Rossmeisl, Enhancing activity for the oxygen evolution reaction: the beneficial interaction of gold with manganese and cobalt oxides, *ChemCatChem* 7 (2015) 149–154, <https://doi.org/10.1002/cctc.201402756>.
- [63] P. Sabatier, Hydrogénations et déshydrogénations par catalyse, *Ber. Dtsch. Chem. Ges.* 44 (1911) 1984–2001, <https://doi.org/10.1002/cber.19110440303>.
- [64] L. Zhuang, L. Ge, Y. Yang, M. Li, Y. Jia, X. Yao, Z. Zhu, Ultrathin iron-cobalt oxide nanosheets with abundant oxygen vacancies for the oxygen evolution reaction, *Adv. Mater.* 29 (2017) 1606793, <https://doi.org/10.1002/adma.201606793>.
- [65] A. Zhao, J. Masa, W. Xia, A. Maljusch, M.-G. Willinger, G. Clavel, K. Xie, R. Schlögl, W. Schuhmann, M. Muhler, Spinel Mn-Co oxide in N-doped carbon nanotubes as a bifunctional electrocatalyst synthesized by oxidative cutting, *J. Am. Chem. Soc.* 136 (2014) 7551–7554, <https://doi.org/10.1021/ja502532y>.
- [66] M.K. Bates, Q. Jia, H. Doan, W. Liang, S. Mukerjee, Charge-transfer effects in Ni-Fe and Ni-Fe-Co mixed-metal oxides for the alkaline oxygen evolution reaction, *ACS Catal.* 6 (2016) 155–161, <https://doi.org/10.1021/acscatal.5b01481>.
- [67] S. Kuboon, Y.H. Hu, Study of NiO-CoO and Co₃O₄-Ni₃O₄ solid solutions in multiphase Ni-Co-O systems, *Ind. Eng. Chem. Res.* 50 (2011) 2015–2020, <https://doi.org/10.1021/ie101249r>.
- [68] A. Sivanantham, S. Shanmugam, Nickel selenide supported on nickel foam as an efficient and durable non-precious electrocatalyst for the alkaline water electrolysis, *Appl. Catal. B: Environ.* 203 (2017) 485–493, <https://doi.org/10.1016/j.apcatb.2016.10.050>.
- [69] R. Zhang, Y.C. Zhang, L. Pan, G.Q. Shen, N. Mahmood, Y.H. Ma, Y. Shi, W. Jia, L. Wang, X. Zhang, W. Xu, J.J. Zou, Engineering cobalt defects in cobalt oxide for highly efficient electrocatalytic oxygen evolution, *ACS Catal.* 8 (2018) 3803–3811, <https://doi.org/10.1021/acscatal.8b01046>.
- [70] A.C. Pebley, E. Decolvenaere, T.M. Pollock, M.J. Gordon, Oxygen evolution on Fe-doped NiO electrocatalysts deposited via microplasma, *Nanoscale* 9 (2017) 15070–15082, <https://doi.org/10.1039/C7NR04302C>.
- [71] E. Arciga-Duran, Y. Meas, J.J. Pérez-Bueno, J.C. Ballesteros, G. Trejo, Effect of oxygen vacancies in electrodeposited NiO towards the oxygen evolution reaction: role of Ni-glycine complexes, *Electrochim. Acta* 268 (2018) 49–58, <https://doi.org/10.1016/j.electacta.2018.02.099>.